

Adaptive Diffusion Models for Motion-corrected Cone-beam Head CT

Antoine De Paepe, Alexandre Bousse, Clémentine Phung-Ngoc, Youness Mellak, Dimitris Visvikis

Abstract—Cone-beam computed tomography (CBCT) is a versatile imaging modality widely used in head and neck diagnostics due to its accessibility and lower radiation dose. However, its relatively long acquisition times make it susceptible to patient motion, especially under sparse-view settings used to reduce dose, which can result in severe image artifacts. In this work, we propose a novel framework, joint reconstruction and motion estimation (JRM) with adaptive diffusion model (ADM), that simultaneously addresses motion compensation and sparse-view reconstruction in head CBCT. Leveraging recent advances in diffusion-based generative models, our method integrates a wavelet-domain diffusion prior into an iterative reconstruction pipeline to guide the solution toward anatomically plausible volumes while estimating rigid motion parameters in a blind fashion. We evaluate our method on simulated motion-affected CBCT data derived from real clinical computed tomography (CT) volumes. Experimental results demonstrate that JRM-ADM substantially improves reconstruction quality over traditional model-based and learning-based baselines, particularly in highly undersampled scenarios. Our approach enables motion-robust and low-dose CBCT imaging, paving the way for improved clinical viability.

Index Terms—Head CBCT, Image Reconstruction, Motion Correction, Adaptive Diffusion Models (ADM)

I. INTRODUCTION

CONE-beam computed tomography (CBCT) has become a valuable imaging modality for head and neck applications. CBCT systems use a flat-panel detector and a cone-shaped X-ray beam to acquire volumetric images in one rotation, and they are now widely used in dental, sinus, and cranial imaging. In these contexts, CBCT often serves as a lower-dose and more accessible alternative to conventional multi-detector computed tomography (CT) [1], [2]. CBCT scanners are also more compact and can be deployed at the point of care (e.g. in outpatient clinics or operating rooms), offering advantages in portability and cost for head imaging [3], [4]. While these features make CBCT particularly appealing, continued efforts are being made to further optimize patient safety—especially in terms of radiation dose.

One strategy to further reduce radiation exposure in head CBCT is to minimize the number of X-ray projections acquired. In general, a standard CBCT might use several hundred projections over 360° , whereas a sparse-view CBCT could

use only a small fraction of those (for instance, under 100 projections). Due to the data incompleteness, the reconstruction problem becomes severely ill-posed, and standard algorithms, such as for example the Feldkamp-Davis-Kress (FDK) [5] algorithm, yields severe streak artifacts. Significant research has addressed the sparse-view reconstruction problem in CT and CBCT. Traditional model-based iterative reconstruction (MBIR) algorithms leverage regularization or prior information to compensate for missing projections. Compressive sensing methods impose sparsity to suppress streak artifacts and recover plausible structures from few-view data [6], [7]. More recently, deep learning (DL) methods have pushed reconstruction quality further. For example, convolutional neural network (CNN) can be trained to refine FDK-reconstructed sparse-view CBCT images [8]. However this kind of supervised methods can have drawbacks, especially when having out-of-distribution data. This limitation has motivated the use of less supervised and more robust alternatives.

On one hand, neural attenuation fields and related approaches [9], [10] have been introduced for sparse view CBCT reconstruction. These methods leverage neural radiance fields—originally designed for synthesizing novel views in computer graphics—to represent the CBCT volume as an implicit neural function. On the other hand, methods at the intersection of MBIR algorithms and DL approaches have been developed. Plug-and-play (PnP) algorithms address image reconstruction inverse problems by integrating a restoration neural network (NN) into iterative processes, often with theoretical convergence guarantees. While early PnP methods used Gaussian denoisers as restoration NN, which are not well-suited for sparse-view CBCT, Vo *et al.* [11] addressed this by training the restoration NN to approximate a proximal operator along a defined optimization trajectory. Finally, diffusion models (DMs) [12] have emerged as state-of-the-art generative approaches capable of learning complex image distributions. Building on the foundational insights of DMs, deep posterior sampling methods [13] have demonstrated remarkable capabilities in denoising, artifact suppression, and even in solving highly ill-posed reconstruction problems in low-dose and three-dimensional (3-D) sparse-view CT [14], [15], where methodology can be extended to sparse-view CBCT.

Nonetheless, all these methods assume a static object and do not account for patient motion during the scan, which is often the case in CBCT given the relatively long acquisition time [16], [17]. Unlike a standard CT scanner that can acquire a head volume in a few seconds, CBCT systems may require 5-60 seconds for a scan [16], during which the patient is expected to remain still. In practice, patients may involuntarily move

This work did not involve human subjects or animals in its research.

All authors declare that they have no known conflicts of interest in terms of competing financial interests or personal relationships that could have an influence or are relevant to the work reported in this paper.

All authors are affiliated to the LaTIM, Inserm, UMR 1101, *Université de Bretagne Occidentale*, Brest, France.

Corresponding author: A. Bousse, bousse@univ-brest.fr

their head or there may be slight shifts in positioning, and even small motions can produce substantial image artifacts, like double contours, ghosting of edges, and overall loss of sharpness and contrast on the reconstructed image [18].

Several strategies have been explored to obtain the motion information needed for motion-corrected (MC) reconstruction. External tracking approaches use additional hardware to track patient motion during the scan. However, a drawback of external systems is the need to accurately register the tracking data with the imaging coordinates. Any misalignment or calibration error between the tracker and the CBCT scanner can reduce the correction accuracy.

Alternatively, data-driven MC reconstruction techniques can estimate the motion directly from the raw data. For example, JRM techniques can jointly estimating the motion from the tomographic projections and reconstructing a motion-free image such that the temporal projections of the registered volume align with the measured ones, [19]–[22]. Autofocus motion correction algorithms, which measure image quality on the reconstructed volume itself, have gained interest in recent years [23]—especially with data-driven quality metrics parameterized by NN [24]–[26]. However, these approaches are not designed to handle sparse-view data. Moreover, in the specific case of learned quality metrics, it can be problematic when motion amplitudes differ from those seen during training.

Despite advances in sparse-view reconstruction and in motion correction, there is a conspicuous gap in methods that tackle both simultaneously, especially in the case of head CBCT. Most prior works compartmentalize the problems: they either assume no motion when dealing with sparse-view data, or assume full-view data when correcting motion. Several studies have explored the integration of limited-angle or sparse-view data with motion compensation in a reconstruction scheme [27], or through DL approaches [28]. However, challenges persist—either in maintaining image quality in the former case or in extending these methods to 3-D applications in the latter. To the best of our knowledge, no existing approach integrates a modern learned-image prior into a JRM framework for the specific case head CBCT. This motivates this work: to offer a new solution that marries the latest advances in generative image modeling with a joint motion-image optimization scheme, to fill this crucial gap.

DMs have arisen as an alternative to generative adversarial networks for image generation and other tasks [29], and have been widely explored in medical imaging [30]. Score-based DMs is a generative technique which consists in training a prior probability distribution function (PDF) by gradually transforming a collection of images into white noise via a stochastic differential equation (SDE), then, in learning the inverse SDE by score matching using a CNN, and finally to generate images from random white noise. Recent advancements in diffusion posterior sampling (DPS) have extended their application to blind inverse problems [31], where the forward operator is unknown, thereby showcasing their versatility and reinforcing the promise of generative approaches in advancing medical imaging reconstruction.

In this paper, we extend our previous JRM in sparse-view context framework [31] for CBCT head CT that leverages

ADMs as a deep posterior sampling prior. Our approach, namely JRM-ADM, integrates a diffusion-based posterior sampling scheme inspired by [32] into an iterative reconstruction algorithm, where the DM acts as a probabilistic regularizer to guide the solution toward anatomically plausible images and the motion is blindly estimated (Figure 1). This joint estimation process allows our algorithm to iteratively refine both the image and the motion parameters until convergence is achieved, thereby reducing motion-induced artifacts while preserving fine anatomical details.

In summary, the main contribution is the first MC sparse-view head CBCT framework, enabling dose reduction while preserving image quality. This is done by introducing a new alternating method, leveraging DMs as a probabilistic regularizer. The advantage of our method is that it can be applied for any geometry and any motion amplitude without retraining the model. To reduce the memory footprint, we introduce wavelet diffusion model which allow to learn a PDF defined on a latent space such that the training of the DM is less memory demanding.

The remainder of this paper is organized as follows: Section II details the theoretical framework and integration of JRM and JRM-ADMs; Section III describes the experimental setup and evaluation metrics and the results; Section IV discusses clinical implications and future research directions; finally, Section V concludes this work.

II. MATERIALS AND METHODS

In the following, all vectors are represented in columns. \cdot^\top denotes the matrix transpose operation. For a given column vector $\mathbf{z} = [z_1, z_2, \dots, z_n]^\top \in \mathbb{R}^n$, $[\mathbf{z}]_i$ denotes the i th entry of \mathbf{z} , i.e., $[\mathbf{z}]_i \triangleq z_i$. $[\mathbf{A}; \mathbf{B}]$ denotes the vertical concatenation of two matrices \mathbf{A} and \mathbf{B} with equal number of columns. Given a positive-definite square matrix \mathbf{A} , we define the norm $\|\cdot\|_{\mathbf{A}}$ by $\|\mathbf{z}\|_{\mathbf{A}} \triangleq \sqrt{\mathbf{z}^\top \mathbf{A} \mathbf{z}}$ where \mathbf{z} is a vector of same dimensions as \mathbf{A} . $\mathbf{0}_{\mathcal{Z}}$ and $\mathbf{I}_{\mathcal{Z}}$ are respectively the zero element and the identity operator in the real vector space \mathcal{Z} .

The 3-D attenuation image to reconstruct is represented by a vector $\mathbf{x} \in \mathbb{R}^m \triangleq \mathcal{X}$ with $m = n_x \cdot n_y \cdot n_z$ voxels

A. Problem Formulation: Joint Reconstruction and Motion Compensation

A CBCT scan operates by rotating an X-ray source and a detector around the patient’s head, capturing a series of two-dimensional projections from various angles $\theta_1, \theta_2, \dots, \theta_{n_a}$, n_a being the number of angles, and we denote by $\mathcal{R}_k: \mathcal{X} \rightarrow \mathcal{Y}$ the X-ray k th line integral operator (i.e., corresponding to angle θ_k), where $\mathcal{Y} \triangleq \mathbb{R}^n$ denotes the projection space with $n = n_h \cdot n_w$ such that each vector of \mathcal{Y} represents a $n_h \times n_w$ projection image. The k th X-ray transmission measurement data is a random vector $\mathbf{y}_k = [y_{1,k}, \dots, y_{n,k}]^\top \in \mathcal{Y}$, which, in absence of electronic noise, follows a Poisson distribution with independent entries given by

$$(y_{i,k} \mid \mathbf{x}) \sim \text{Poisson}(\bar{y}_{i,k}(\mathbf{x})) \quad (1)$$

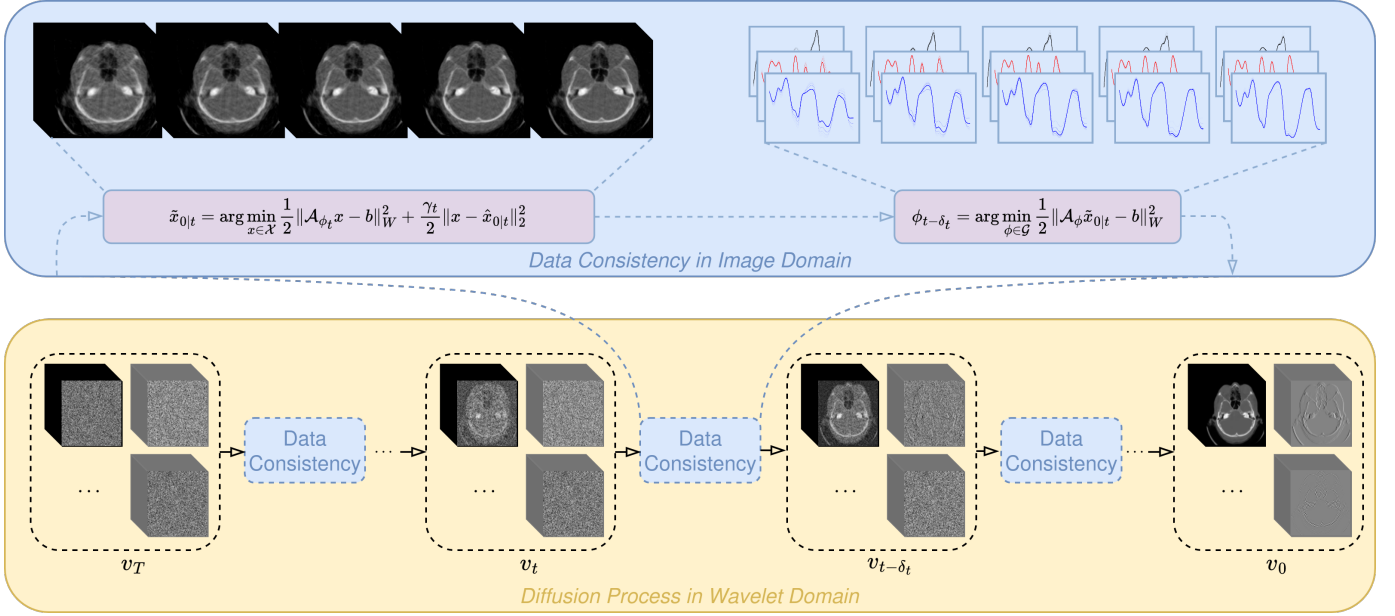


Fig. 1: Overview of the proposed JRM-ADM approach.

where $\bar{y}_{i,k}(\mathbf{x}) \triangleq \mathbb{E}[y_{i,k} | \mathbf{x}]$ is the conditional expected number of detected given \mathbf{x} , which is given by the Beer-Lambert law (assuming the X-ray source in monochromatic):

$$\bar{y}_{i,k}(\mathbf{x}) = I \cdot e^{-[\mathcal{R}_k(\mathbf{x})]_i} \quad (2)$$

Given the entire measurement dataset $\mathbf{y} \triangleq [\mathbf{y}_1; \dots; \mathbf{y}_{n_a}] \in \mathcal{Y}^{n_a}$, image reconstruction can be achieved by finding the maximum *a posteriori* (MAP) estimate of \mathbf{x} , i.e.,

$$\max_{\mathbf{x} \in \mathcal{X}} p(\mathbf{y} | \mathbf{x}) \cdot p(\mathbf{x}) \quad (3)$$

where the conditional PDF $p(\mathbf{y} | \mathbf{x})$ is given (1) and $p(\mathbf{x})$ is a prior PDF on \mathbf{x} , which is generally unknown and replaced (in its post-log form) by a regularizer promoting image piecewise smoothness. Solving (3) can be achieved with optimization transfer algorithm [33] when $p(\mathbf{x})$ is differentiable, or with primal-dual algorithms [34] when $p(\mathbf{x})$ is not differentiable (e.g. total variation (TV)).

The acquisition of the data $\mathbf{y} \triangleq [\mathbf{y}_1; \dots; \mathbf{y}_{n_a}] \in \mathcal{Y}^{n_a}$ is performed over a time interval $[0, T]$ during which the head is subject to motion, thus creating inconsistencies between the \mathbf{y}_k s. In the following we assume there is no intra-projection motion (i.e., each \mathbf{y}_k is an instant snapshot of the patient's head), and we denote by $t_k, k = 1, \dots, n_a$, the time at which the k th projection occurs, with $t_1 = 0$ and $t_{n_a} = T$. At each time $t \in [0, T]$, the support of the attenuation image \mathbf{x} is affected by a 3-D rigid motion of given by a time-dependent parameter $\omega(t) = [\omega_1(t), \dots, \omega_6(t)]$

$$[\omega_1(t), \omega_2(t), \omega_3(t)] = [\vartheta_x(t), \vartheta_y(t), \vartheta_z(t)] \triangleq \boldsymbol{\vartheta}(t) \quad (4)$$

$$[\omega_4(t), \omega_5(t), \omega_6(t)] = [\tau_x(t), \tau_y(t), \tau_z(t)] \triangleq \boldsymbol{\tau}(t) \quad (5)$$

where $\boldsymbol{\vartheta}(t) \in [0, 2\pi]^3$ is the vector of the rotation angles around each axis and $\boldsymbol{\tau}(t)$ is the translation vector. Furthermore, we denote by $\mathcal{W}_{\omega(t)}: \mathcal{X} \rightarrow \mathcal{X}$ denotes the image-to-image transformation (i.e., a warping matrix, see for example Bousse

et al. [19]) associated to the rigid transformation of parameter $\omega(t)$.

To preserve motion smoothness, we introduce a temporal regularization by modeling each component of $\omega(t)$ using cubic B-splines:

$$\omega_p(t) = \sum_{i=1}^{n_c} \phi_{i,p} B\left(\frac{t - s_i}{r}\right) \quad \forall p = 1, \dots, 6 \quad (6)$$

where $B: \mathbb{R} \rightarrow \mathbb{R}$ is the cubic B-spline basis functions, $s_i, i = 1, \dots, n_c$ are the n_c uniformly distributed control points with $s_1 = 0$ and $s_{n_c} = T$ (not to be mistaken with the acquisition times $t_k, k = 1, \dots, n_c$), r is the distance between control points and $\phi = \{\phi_{i,p}\}_{i,p=1}^{n_c,6}$. Furthermore, we define $\mathcal{W}_{\phi,k}: \mathcal{X} \rightarrow \mathcal{X}$ the image-to-image transformation operator of parameter ϕ at time t_k corresponding to the k th CBCT projection:

$$\mathcal{W}_{\phi,k} \triangleq \mathcal{W}_{\omega(t_k)} \quad (7)$$

where ω is defined as (6).

With introduction of the motion defined by ϕ , the forward model given by (1) and (2) can be redefined as

$$(y_{i,k} | \mathbf{x}, \phi) \sim \text{Poisson}(\bar{y}_{i,k}(\mathbf{x}, \phi)) \quad (8)$$

with $\bar{y}_{i,k}(\mathbf{x}) \triangleq \mathbb{E}[y_{i,k} | \mathbf{x}, \phi]$ defined as

$$\bar{y}_{i,k}(\mathbf{x}, \phi) = I \cdot e^{-[\mathcal{R}_k \circ \mathcal{W}_{\phi,k}(\mathbf{x})]_i} \quad (9)$$

In absence of prior on ϕ , MC reconstruction of the image \mathbf{x} from the measurement \mathbf{y} can be achieved by performing JRM though a MAP optimization problem

$$\max_{\mathbf{x} \in \mathcal{X}, \phi \in \mathcal{C}} p(\mathbf{y} | \mathbf{x}, \phi) \cdot p(\mathbf{x}) \quad (10)$$

where the conditional PDF $p(\mathbf{y} | \mathbf{x}, \phi)$ is given by (8) and (9), and $\mathcal{C} = \mathbb{R}^{n_c \times 6}$ denotes the set of B-spline coefficients ϕ modeling the rigid motion. Defining the MC projector \mathcal{A}_{ϕ} as

$$\mathcal{A}_{\phi} \triangleq [\mathcal{R}_1 \circ \mathcal{W}_{\phi,1}; \dots; \mathcal{R}_1 \circ \mathcal{W}_{\phi,n_a}]: \mathcal{X} \rightarrow \mathcal{Y}^{n_a}, \quad (11)$$

a weighted least squares approximate of $-\log(p(\mathbf{y}|\mathbf{x}, \phi))$ is [33]

$$-\log p(\mathbf{y}|\mathbf{x}, \phi) \approx \|\mathcal{A}_\phi(\mathbf{x}) - \mathbf{b}\|_{\mathbf{W}}^2 + C \quad (12)$$

where C is independent of \mathbf{x} and ϕ , $\mathbf{b} \triangleq [b_1; \dots; b_{n_a}]$, $b_k \triangleq [b_{1,k}, \dots, b_{n,k}]$ and $b_{i,k} \triangleq \log I/y_{i,k}$ (assuming $y_{i,k} > 0$ for all i, k), and (10) is approximated in its post-log form as

$$\min_{\mathbf{x} \in \mathcal{X}, \phi \in \mathcal{C}} \|\mathcal{A}_\phi(\mathbf{x}) - \mathbf{b}\|_{\mathbf{W}}^2 + \beta R(\mathbf{x}) \quad (13)$$

where $R: \mathbb{R} \rightarrow \mathbb{R}$ is a convex regularizer playing the role of $-\log p(\mathbf{x})$ and $\beta > 0$ controls the strength of R . Solving (13) is a standard JRM optimization problem which can be found in the literature in different forms [19]–[22].

B. Joint Reconstruction and Motion Estimation with Diffusion Models

In the following, $t = 1, \dots, T$ denotes the diffusion index and should not be mistaken with the acquisition time from Section II-A.

1) *Background on Diffusion Models:* In absence of a tractable prior PDF $p(\mathbf{x})$, \mathbf{x} can be sampled through a model trained through diffusion.

A commonly adopted approach is the denoising diffusion probabilistic model [35], which samples \mathbf{x}_t given \mathbf{x}_{t-1} , $t = 1, \dots, T$, starting from an initial image \mathbf{x}_0 sampled from the training dataset with PDF p^{data} ,

$$\mathbf{x}_t = \sqrt{\alpha_t} \mathbf{x}_{t-1} + \sqrt{1 - \alpha_t} \epsilon_t \quad (14)$$

where $\epsilon_t \sim \mathcal{N}(\mathbf{0}_{\mathcal{X}}, \mathbf{I}_{\mathcal{X}})$ and α_t is a scaling factor decreasing from $\alpha_0 = 1$ to $\alpha_T = 0$ such that $\mathbf{x}_T \sim \mathcal{N}(\mathbf{0}_{\mathcal{X}}, \mathbf{I}_{\mathcal{X}})$. One prominent sampling algorithm, denoising diffusion implicit model (DDIM) [36], approximates the reverse process to sample an image from a generalized version of $p^{\text{data}}(\mathbf{x})$ that approximates the theoretical prior $p(\mathbf{x})$, with the following update rule:

$$\begin{aligned} \mathbf{x}_{t-1} &= \sqrt{\bar{\alpha}_{t-1}} \hat{\mathbf{x}}_{0|t} + \sqrt{1 - \bar{\alpha}_{t-1} - \sigma_t^2} \cdot \frac{\mathbf{x}_t - \sqrt{\bar{\alpha}_t} \hat{\mathbf{x}}_{0|t}}{\sqrt{1 - \bar{\alpha}_{t-1}}} \\ &+ \sigma_t^2 \epsilon_t, \quad \epsilon_t \sim \mathcal{N}(\mathbf{0}_{\mathcal{X}}, \mathbf{I}_{\mathcal{X}}) \end{aligned} \quad (15)$$

where $\bar{\alpha}_t = \prod_{s=1}^t \alpha_s$, $\sigma_t = \sqrt{1 - \alpha_t} \sqrt{1 - \bar{\alpha}_{t-1}} / \sqrt{1 - \bar{\alpha}_t}$ and $\hat{\mathbf{x}}_{0|t} \triangleq \mathbb{E}[\mathbf{x}_0 | \mathbf{x}_t]$ is given by Tweedie's formula,

$$\hat{\mathbf{x}}_{0|t} = \frac{1}{\sqrt{\bar{\alpha}_t}} (\mathbf{x}_t + (1 - \bar{\alpha}_t) \nabla \log p_t(\mathbf{x}_t)), \quad (16)$$

p_t being the PDF of \mathbf{x}_t . The score function $\nabla_{\mathbf{x}_t} \log p_t(\mathbf{x}_t)$ is untractable and therefore $\hat{\mathbf{x}}_{0|t}$ is approximated through a NN $\mathbf{x}_\eta: \mathcal{X} \times [0, T] \rightarrow \mathcal{X}$ with parameter vector η trained to recover \mathbf{x}_0 from \mathbf{x}_t as

$$\min_{\eta} \mathbb{E}_{t, \mathbf{x}_0, \mathbf{x}_t} \left[\|\mathbf{x}_\eta(\mathbf{x}_t, t) - \mathbf{x}_0\|_2^2 \right], \quad (17)$$

where $t \sim \mathcal{U}[0, T]$, $\mathbf{x}_0 \sim p^{\text{data}}$, and $\mathbf{x}_t \sim \mathcal{N}(\sqrt{\bar{\alpha}_t} \mathbf{x}_0, (1 - \bar{\alpha}_t) \mathbf{I}_{\mathcal{X}})$.

2) *Diffusion Models in Wavelet Transform Domain:* Applying DMs to 3-D medical imaging poses significant challenges due to high computational cost and memory footprint. To mitigate these issues, latent diffusion models operate in a compressed latent space. Recent studies have proposed performing the diffusion process in the wavelet domain [37], which substantially reduces memory requirements during both training and inference while achieving state-of-the-art performance.

In this context, an orthogonal discrete wavelet transform $\mathcal{V}: \mathcal{X} \rightarrow \mathcal{V} \triangleq \mathbb{R}^{8 \times \frac{n_x}{2} \times \frac{n_y}{2} \times \frac{n_z}{2}}$, with $\mathcal{V}^{-1} = \mathcal{V}^\top$, is employed to decompose the 3-D image \mathbf{x} into an eight-channel wavelet coefficient image \mathbf{v} that has half the spatial resolution in each dimension compared to \mathbf{x} . The orthogonality of \mathcal{V} ensures a lossless transition between the wavelet domain \mathcal{V} and the original image domain \mathcal{X} . Specifically, the diffusion process described in (14) can be reformulated in the wavelet domain as

$$\underbrace{\mathcal{V} \mathbf{x}_t}_{\mathbf{v}_t} = \sqrt{\alpha_t} \underbrace{\mathcal{V} \mathbf{x}_{t-1}}_{\mathbf{v}_{t-1}} + \sqrt{1 - \alpha_t} \underbrace{\mathcal{V} \epsilon_t}_{\tilde{\epsilon}_t}, \quad (18)$$

with $\epsilon_t \sim \mathcal{N}(\mathbf{0}_{\mathcal{X}}, \mathbf{I}_{\mathcal{X}})$ so that $\tilde{\epsilon}_t \triangleq \mathcal{V} \epsilon_t \sim \mathcal{N}(\mathbf{0}_{\mathcal{V}}, \mathbf{I}_{\mathcal{V}})$ as \mathcal{V} is orthogonal.

Thus, training a NN $\mathbf{v}_\eta: \mathcal{V} \times [0, T] \rightarrow \mathcal{V}$ can be trained in a similar fashion as in (17) (in the wavelet domain \mathcal{V}) to predict \mathbf{v}_0 from \mathbf{v}_t is can be utilized to predict \mathbf{x}_0 from \mathbf{x}_t through \mathcal{V}^{-1} .

3) *Diffusion Posterior Sampling for Blind Inverse Problems:* DMs can be used for CBCT MC image reconstruction, with incorporation of a time-dependent rigid motion parametrized by ϕ_t (cf. (6)), using the conditional score and assuming ϕ_t and $[\mathbf{x}_0, \dots, \mathbf{x}_T]$ are independent (which is an acceptable assumption for rigid motion):

$$\nabla_{\mathbf{x}_t} \log p(\mathbf{x}_t | \mathbf{y}, \phi_t) = \nabla_{\mathbf{x}_t} \log p_t(\mathbf{x}_t) + \nabla_{\mathbf{x}_t} \log p(\mathbf{y} | \mathbf{x}_t, \phi_t), \quad (19)$$

The DPS framework use the following approximation [13]:

$$\nabla_{\mathbf{x}_t} \log p(\mathbf{y} | \mathbf{x}_t, \phi_t) \approx \nabla_{\mathbf{x}_t} \log p(\mathbf{y} | \hat{\mathbf{x}}_{0|t}(\mathbf{x}_t), \phi_t) \quad (20)$$

where the log-conditional PDF $\log p(\mathbf{y} | \hat{\mathbf{x}}_{0|t}, \phi_t)$ is given by (12) with $\mathbf{x} = \hat{\mathbf{x}}_{0|t}$. However, computing such a gradient is not always possible, especially in large scale inverse problems due the memory footprint. Alternative solutions have been proposed, such as the manifold preserving guided diffusion shortcut approach [38]:

$$\nabla_{\mathbf{x}_t} \log p(\mathbf{y} | \hat{\mathbf{x}}_{0|t}(\mathbf{x}_t), \phi_t) \approx \nabla_{\mathbf{x}_{0|t}} \log p(\mathbf{y} | \hat{\mathbf{x}}_{0|t}, \phi_t) \quad (21)$$

Another approximation can be derived from the conditional version of Tweedie's formula

$$\begin{aligned} \mathbb{E}[\mathbf{x}_0 | \mathbf{x}_t, \mathbf{y}, \phi_t] &= \mathbb{E}[\mathbf{x}_0 | \mathbf{x}_t] \\ &+ \frac{1 - \bar{\alpha}_t}{\sqrt{\bar{\alpha}_t}} \nabla_{\mathbf{x}_t} \log p(\mathbf{y} | \mathbf{x}_t, \phi_t) \end{aligned} \quad (22)$$

Combined with the approximation (21), this formula resembles a gradient ascent step starting from $\hat{\mathbf{x}}_{0|t} = \mathbb{E}[\mathbf{x}_0 | \mathbf{x}_t]$ to mini-

mize $\log p(\mathbf{y}|\mathbf{x}, \phi)$. This observation motivates the utilization of the following proximal approximation [32], [39]:

$$\begin{aligned} \mathbb{E}[\mathbf{x}_0 | \mathbf{x}_t, \mathbf{y}] &\approx \arg \min_{\mathbf{x} \in \mathcal{X}} \frac{1}{2} \|\mathcal{A}_\phi(\mathbf{x}) - \mathbf{b}\|_{\mathbf{W}}^2 + \frac{\gamma_t}{2} \|\mathbf{x} - \hat{\mathbf{x}}_{0|t}\|_2^2 \\ &\triangleq \tilde{\mathbf{x}}_{0|t}. \end{aligned} \quad (23)$$

Meanwhile, the motion parameter ϕ_{t-1} can be updated by solving

$$\phi_{t-1} = \arg \min_{\phi \in \mathcal{C}} \frac{1}{2} \|\mathcal{A}_\phi(\tilde{\mathbf{x}}_{0|t}) - \mathbf{b}\|_{\mathbf{W}}^2 \quad (24)$$

which can be solved with any iterative algorithm initialized from ϕ_t .

Finally, expected wavelet coefficient $\tilde{\mathbf{v}}_{0|t}$ are extracted from $\tilde{\mathbf{x}}_{0|t}$, i.e.,

$$\tilde{\mathbf{v}}_{0|t} \leftarrow \mathcal{V}(\tilde{\mathbf{x}}_{0|t}) \quad (25)$$

and the new wavelet coefficient \mathbf{v}_t are sampled using the DDIM update (15) with $\tilde{\mathbf{v}}_{0|t}$ replacing $\hat{\mathbf{x}}_{0|t}$ and $\sigma_t = 0$ as proposed in Song *et al.* [36].

The overall approach, namely JRM-ADM, is summarized in Algorithm 1. Similarly to Song *et al.* [36], we used a time step $\delta_t > 1$ to speed up the sampling. Additionally, we implemented an accelerated version using the jumpstart strategy, namely JRM-ADM_{js}, proposed in Jiang *et al.* [40], using a pre-estimated image and motion prestimated by solving (13) without regularizer.

Algorithm 1 Pseudo code of JRM-ADM.

Require: $T, \mathbf{y}, \{\gamma_t\}_{t=1}^T, \{\delta_t\}_{t=1}^T, \{\alpha_t\}_{t=1}^T$
1: $t \leftarrow T$
2: $\epsilon \sim \mathcal{N}(\mathbf{0}_{\mathcal{V}}, \mathbf{I}_{\mathcal{V}})$
3: $\mathbf{v}_t \leftarrow \epsilon$
4: $\phi_t \leftarrow \mathbf{0}_{\mathcal{C}}$
5: **while** $t > 0$ **do**
6: $\hat{\mathbf{v}}_{0|t} \leftarrow \mathbf{v}_{\eta}(\mathbf{v}_t, t)$
7: $\hat{\mathbf{x}}_{0|t} \leftarrow \mathcal{V}^{-1}(\hat{\mathbf{v}}_{0|t})$
8: $\hat{\mathbf{x}}_{0|t} \leftarrow \arg \min_{\mathbf{x} \in \mathcal{X}} \frac{1}{2} \|\mathcal{A}_{\phi_t}(\mathbf{x}) - \mathbf{b}\|_{\mathbf{W}}^2 + \frac{\gamma_t}{2} \|\mathbf{x} - \hat{\mathbf{x}}_{0|t}\|_2^2$
9: $\phi_{t-\delta_t} \leftarrow \arg \min_{\phi \in \mathcal{C}} \frac{1}{2} \|\mathcal{A}_\phi(\hat{\mathbf{x}}_{0|t}) - \mathbf{b}\|_{\mathbf{W}}^2$
10: $\tilde{\mathbf{v}}_{0|t} \leftarrow \mathcal{V}(\hat{\mathbf{x}}_{0|t})$
11: $\mathbf{v}_{t-\delta_t} \leftarrow \sqrt{\alpha_{t-\delta_t}} \tilde{\mathbf{v}}_{0|t} + \sqrt{1 - \alpha_{t-\delta_t}} \cdot \frac{\mathbf{v}_t - \sqrt{\alpha_t} \tilde{\mathbf{v}}_{0|t}}{\sqrt{1 - \alpha_{t-\delta_t}}}$
12: $t = t - \delta_t$
13: **end while**
14: $\hat{\mathbf{x}}_0 = \mathcal{V}^{-1}(\hat{\mathbf{v}}_{0|t})$
15: **return** $\hat{\mathbf{x}}_0, \phi_0$

III. RESULTS

A. Data Preparation

We utilize the CQ500 dataset [41], which comprises 491 multi-detector computed tomography scans collected from patients presenting with symptoms of head trauma or stroke. From the full dataset, we select a subset of 298 volumes that satisfy two main criteria: (1) a sufficient number of axial slices, and (2) a small slice thickness, ensuring appropriate resolution for simulation of cone-beam acquisition. The selected volumes

are clipped in between -1000 and 2000 Hounsfield units and divided into training, validation, and test sets with 263, 15, and 20 samples, respectively. The validation set is used during model training and to finetune sampling hyperparameters.

We trained the NN \mathbf{v}_{η} using the ADAM optimizer for approximately 1.2 million iterations, using rotations and translations for data augmentation. The training was performed on volumes normalized to the range $[-1, 1]$. This normalization is explicitly incorporated into the forward model (9) while performing JRM-ADM.

We simulated realistic motion-affected CBCT acquisitions following (8) and (9) with $I = 5 \cdot 10^5$, ground truth (GT) volumes $\mathbf{x} = \mathbf{x}^*$ from the testing dataset and random GT motion B-spline parameters $\phi = \mathbf{x}^*$ tuned to generate a continuous motion following (6) (with 20 control points s_i) with translations in the range of $[-5, 5]$ mm and rotations in the range of $[-5, 5]$ degrees.

For each scan, we generated 120 projections uniformly distributed across $[0, 2\pi]$ using the cone-beam projector implemented in the Carterbox GitHub repository¹ (a fork of TorchRadon [42]). The acquisition geometry includes a source-to-isocenter distance of 785 mm, a source-to-detector distance of 1,200 mm, with 500×700 detector pixels and an isotropic pixel size of 0.5 mm.

From this projections, we uniformly sampled the desired number of views $s \in \{20, 40, 60\}$ needed for the reconstruction, enabling to compare a same motion applied to different level of sparse-view setting. Reconstructions were performed on a 3-D grid with isotropic voxel spacing of $1 \times 1 \times 1$ mm, within volumes of size $160 \times 192 \times 192$ voxels.

B. Experiment settings

For performance comparison, we use standard FDK reconstruction as a baseline. As a model-based approach, we employ JRM (13) using TV regularization for R . The regularization strength β is adjusted according to the number of projections: $\beta = 3 \cdot 10^3$ for 60 projections, $\beta = 1.5 \cdot 10^3$ for 40 projections, and $\beta = 7.5 \cdot 10^2$ for 20 projections.

We then evaluated our proposed and ADM-JRM and ADM-JRM_{js}, with $T = 400$ and $\delta_t = 10$. The initial estimation of the volume and motion parameters is performed using an alternating optimization scheme over the volume \mathbf{x} and the motion parameters ϕ . Each sub-problem is optimized using RMSPROP with 15 gradient steps, repeated for 10 alternating iterations. Within Algorithm 1, each sub-problem is optimized using 5 steps of the RMSPROP algorithm. At each diffusion step t , the optimization is initialized with the estimate obtained from the previous iteration. The diffusion regularization strength γ_t is fixed over time and set according to the number of projections: $\gamma_t = 2 \times 10^4$ (60 projections), 4×10^4 for (40 projections), and 6×10^4 (20 projections).

For the full ADM-JRM pipeline, we set $T = 1000$ diffusion steps and maintain $\delta_t = 10$. During the first 10 iterations, we disabled diffusion regularization by setting $\gamma_t = 0$ across all sampling conditions. In this initialization phase, the volume and motion estimation are performed with 15 RMSPROP steps.

¹<https://github.com/carterbox/torch-radon>

For the remaining diffusion steps t , we set $\gamma_t = 9 \times 10^3$ (60 projections), $\gamma_t = 1 \times 10^4$ (40 projections), and $\gamma_t = 1.1 \times 10^4$ (20 projections). The minimization steps again use five RMSPROP iterations per diffusion update.

To ensure temporal alignment across different sparse-view scenarios $s \in \{20, 40, 60\}$, we select the central projection angle, indexed by k_s , as the reference frame for warping, corresponding to the acquisition angle $\theta_{k_s} = \pi$. We then compared the warped reconstructed images $\mathcal{W}_{\phi, k_s} \mathbf{x}$ (except for FDK which has no motion compensation) with the GT image $\mathcal{W}_{\phi^*, k_s} \mathbf{x}^*$. We use the peak signal-to-noise ratio (PSNR) and structural similarity index measure (SSIM) as quantitative metrics for evaluation. We also report the mean absolute error (MAE) on both translations and rotations to evaluate the accuracy of the estimated motion.

C. Full-view Preliminary Results

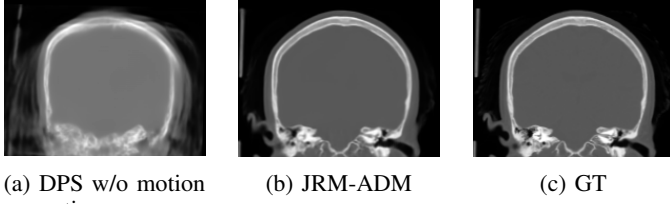


Fig. 2: GT and reconstructed volumes, with and without motion compensation, in the 80-view setting.

We first conducted a preliminary experiment to assess the effect of motion in a DPS framework. For this experiment, we considered the 120 views and we compared JRM-ADM with standard DPS, i.e., Algorithm 1 with $\phi = \mathbf{0}_C$.

The results are shown in Figure 2. The DPS-reconstructed image exhibits pronounced motion artifacts, such as blurring and double edges and distortions of the general shape, while JRM-ADM-reconstructed volume appears similar to the GT volume.

This observation highlights the importance of explicitly modeling and compensating for motion as part of the DPS reconstruction pipeline to achieve accurate results.

D. Sparse-view Experiments Results

Reconstructed images for varying numbers of projections and GT volume are presented in Figure 3 for one patient with $s \in \{20, 40, 60\}$ (axial plane) and in Figure 4 on another patient with $s = 20$ (sagittal and coronal planes).

The FDK-based reconstructions exhibit noise and pronounced streak artifacts, which become increasingly severe as the number of projections decreases. This reduction in number of views leads to a significant loss of structural information. Additionally, motion artifacts degrade image quality, leading to a reduction in fine details.

The JRM-TV reconstructions demonstrate a correct capacity for motion compensation and accurate volume estimation, particularly in the 60-view setting, resulting in sharp and high-quality images. However, as the number of projections

Views	Method	PSNR (\uparrow)	SSIM (\uparrow)	MAE τ (\downarrow)	MAE ϑ (\downarrow)
60	FDK	17.00	0.23	-	-
	JRM-TV	28.91	0.90	0.34	0.11
	JRM-ADM _{js}	30.15	0.93	0.18	0.11
	JRM-ADM	29.67	0.92	0.27	0.09
40	FDK	16.92	0.19	-	-
	JRM-TV	27.19	0.87	0.43	0.12
	JRM-ADM _{js}	28.75	0.91	0.20	0.12
	JRM-ADM	28.66	0.91	0.29	0.11
20	FDK	14.96	0.14	-	-
	JRM-TV	23.38	0.75	0.86	0.17
	JRM-ADM _{js}	25.15	0.82	0.33	0.18
	JRM-ADM	27.18	0.87	0.30	0.12

TABLE I: Quantitative results of methods in comparison on the CQ500 dataset for the MC reconstruction tasks under sparse view settings of 60, 40, and 20 views. The best and second-best results are highlighted in bold.

decreases, the reconstructions exhibit both increased streak artifacts and over smoothed area, leading to a general loss of detail, with fine structures becoming less discernible.

The JRM-ADM_{js} and JRM-ADM methods exhibit similarly high levels of detail in both the 60-view and 40-view scenarios, significantly outperforming JRM-TV in terms of accuracy, as reflected by higher PSNR and SSIM value as shown in Table I. Fine details in the nasal region are accurately preserved and motion is fully compensated.

However, in the more challenging 20-view case, JRM-ADM outperforms JRM-ADM_{js}, with the latter showing a tendency to hallucinate structures. While motion is generally well estimated—supported by low MAE in both translations and rotations—this degradation can be attributed to an insufficient number of refinement steps in JRM-ADM_{js}, which becomes particularly limiting under the highly ill-posed conditions of ultra sparse-view motion affected reconstructions.

Regarding motion estimation, JRM-ADM and JRM-ADM_{js} tend to yield more accurate motion estimates compared to JRM-TV, as illustrated in Figure 5. This improved estimation facilitates the diffusion process in refining fine image details, contributing to overall reconstruction quality.

IV. DISCUSSION

This study highlights the potential of ADMs for motion corrected sparse-view head CBCT imaging. That said, several limitations still need to be addressed before this approach can be fully applied in real-world clinical settings.

Although the CT volumes we used are based on real acquisitions, we do not have direct access to the corresponding raw projection data. Hence, while we simulate realistic conditions such as Poisson noise and sparse-view acquisition, we did not take into account for real-world effects, such as scatter or beam hardening. These factors can impact image quality and reconstruction fidelity in clinical practice, highlighting the need to validate our method on real projection data.

One major challenge lies in the computational cost requirements of the method. For example, running a 40-view ADM-JRM diffusion process takes about 20 minutes, which is not suitable for urgent clinical scenarios where rapid diagnosis is

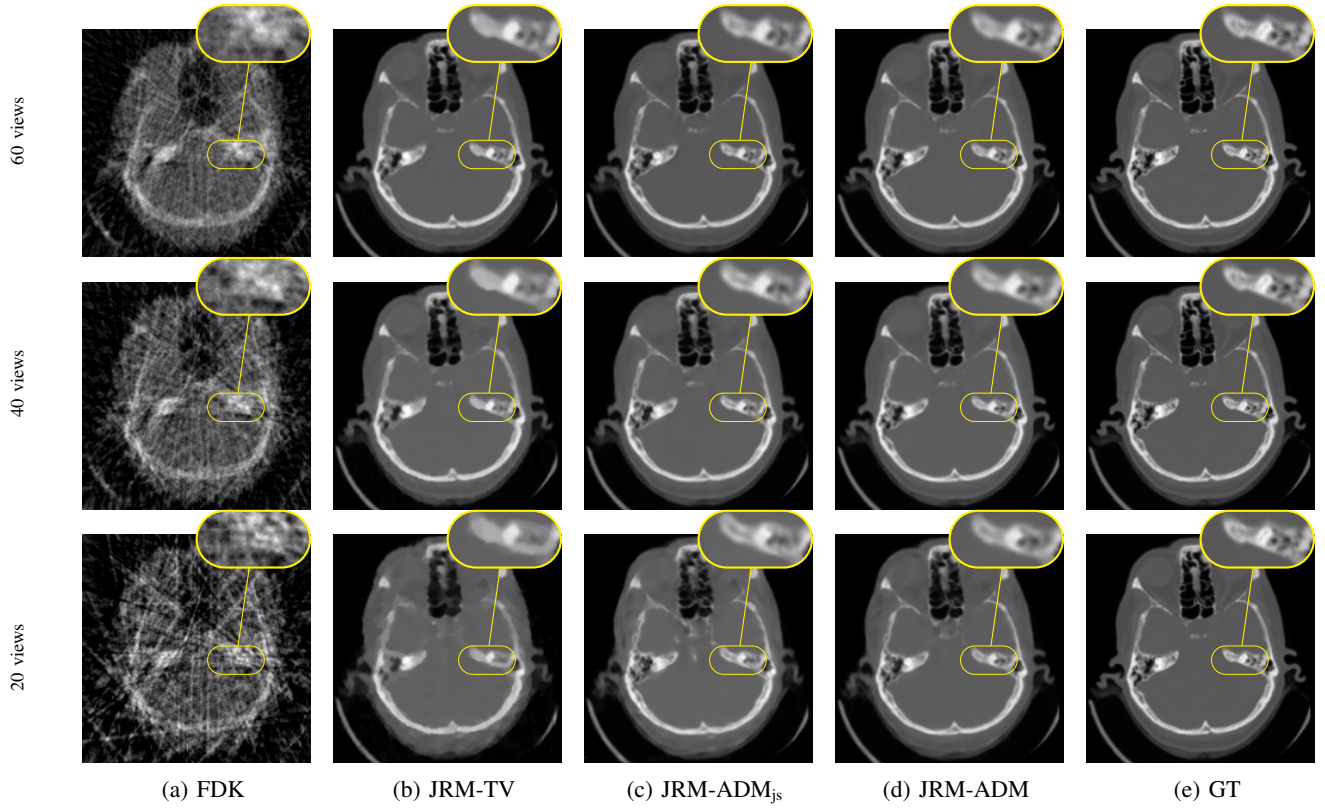


Fig. 3: GT and reconstructed volumes (axial plane) for sparse-view CBCT: results are shown for 60-, 40-, and 20-view acquisition settings.

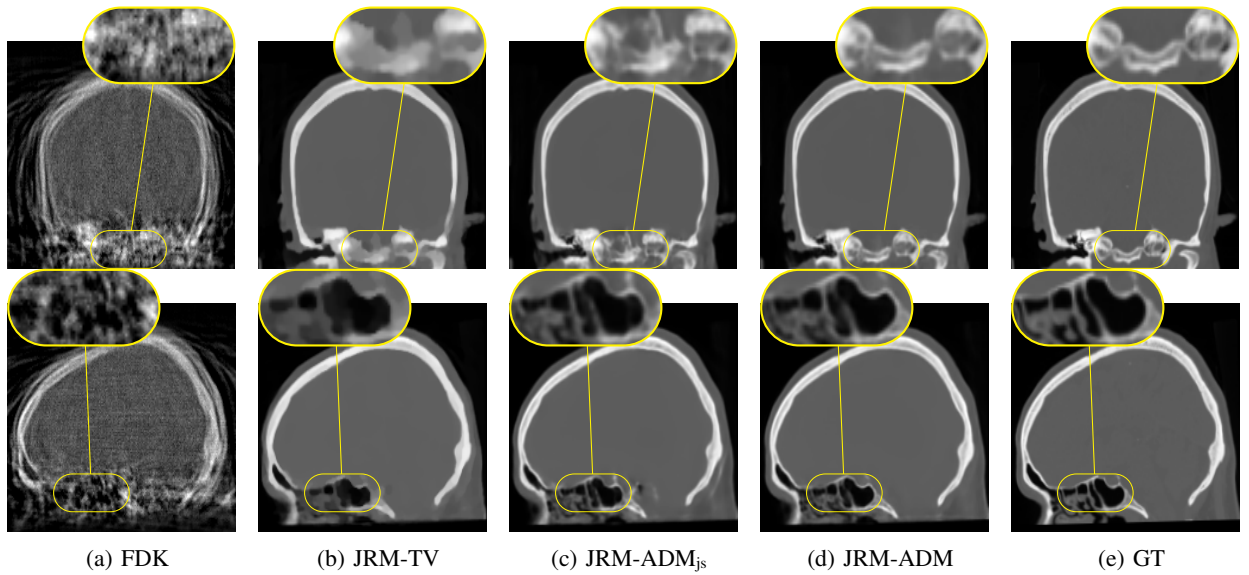


Fig. 4: GT and reconstructed volumes (coronal and sagittal planes) in the 20-view sparse CBCT setting.

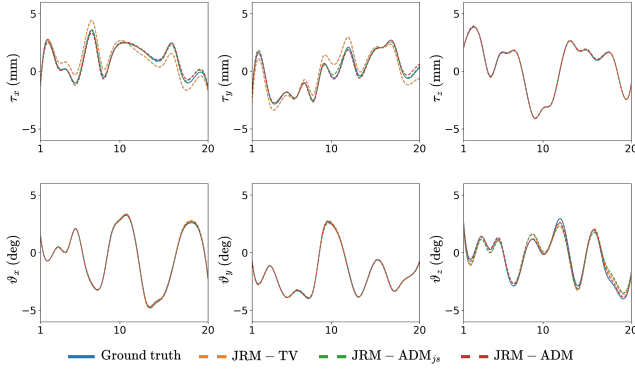


Fig. 5: Estimated motion patterns obtained using JRM-based methods in the 20-view setting, shown alongside the ground truth motion of the patient from Figure 3.

crucial, particularly in life-threatening situations. Our approach is currently better suited for follow-up cases.

To address this limitation, two potential strategies can be considered. First, motion estimation could be performed at a lower resolution than that of the reconstructed volume, which would reduce computational cost but may result in the loss of fine structural details. Second, incorporating differentiable X-ray rendering techniques—such as DiffDRR [43]—could enable direct optimization over the forward model’s geometry. This approach has the potential to eliminate the need for explicit volume warping followed by projection, thereby improving computational efficiency.

V. CONCLUSION

In this work, we addressed sparse-view head CBCT image reconstruction with motion compensation. While prior research has made substantial progress in either sparse-view reconstruction or motion correction independently, our approach is the first to combine these two aspects within a single framework in the context of head CBCT, building upon our previous work on sparse-view 4DCT. By integrating a diffusion-based prior in a blind fashion, we enable robust reconstruction across arbitrary geometries and rigid motion patterns, while preserving fine anatomical details even under severely sparse acquisition conditions. Our proposed framework opens a promising path toward safer, lower-dose, and artifact-resistant CBCT imaging for the head, with strong potential for routine clinical practice.

REFERENCES

- [1] G. Li, “Patient radiation dose and protection from cone-beam computed tomography,” *Imaging Science in Dentistry*, vol. 43, no. 2, pp. 63–69, Jun. 2013, ISSN: 2233-7822. DOI: 10.5624/isd.2013.43.2.63. [Online]. Available: <https://www.ncbi.nlm.nih.gov/pmc/articles/PMC3691375/> (visited on 04/14/2025).
- [2] P. Nicholson, N. M. Cancelliere, J. Bracken, E. Hummel, F. van Nijnatten, P. Withagen, P. van de Haar, B. Hallacoglu, M. van Vlimmeren, R. Agid, T. Krings, and V. Mendes Pereira, “Novel flat-panel cone-beam CT compared to multi-detector CT for assessment of acute ischemic stroke: A prospective study,” *European Journal of Radiology*, vol. 138, p. 109 645, May 2021, ISSN: 1872-7727. DOI: 10.1016/j.ejrad.2021.109645.
- [3] Z. Rumboldt, W. Huda, and J. W. All, “Review of portable CT with assessment of a dedicated head CT scanner,” *AJNR. American journal of neuroradiology*, vol. 30, no. 9, pp. 1630–1636, Oct. 2009, ISSN: 1936-959X. DOI: 10.3174/ajnr.A1603.

- [4] P. Wu, A. Sisniega, J. W. Stayman, W. Zbijewski, D. Foos, X. Wang, N. Khanna, N. Aygun, R. D. Stevens, and J. H. Siewerdsen, “Cone-beam CT for imaging of the head/brain: Development and assessment of scanner prototype and reconstruction algorithms,” *Medical Physics*, vol. 47, no. 6, pp. 2392–2407, Jun. 2020, ISSN: 2473-4209. DOI: 10.1002/mp.14124.
- [5] L. A. Feldkamp, L. C. Davis, and J. W. Kress, “Practical cone-beam algorithm,” *JOSA A*, vol. 1, no. 6, pp. 612–619, Jun. 1, 1984, Publisher: Optica Publishing Group, ISSN: 1520-8532. DOI: 10.1364/JOSAA.1.000612. [Online]. Available: <https://opg.optica.org/josaa/abstract.cfm?uri=josaa-1-6-612> (visited on 04/12/2025).
- [6] S. Boyd, “Distributed optimization and statistical learning via the alternating direction method of multipliers,” *Foundations and Trends® in Machine Learning*, vol. 3, no. 1, pp. 1–122, 2010, ISSN: 1935-8237, 1935-8245. DOI: 10.1561/22000000016. [Online]. Available: <http://www.nowpublishers.com/article/Details/MAL-016> (visited on 04/12/2025).
- [7] A. Chambolle and T. Pock, “A first-order primal-dual algorithm for convex problems with applications to imaging,” *Journal of Mathematical Imaging and Vision*, vol. 40, no. 1, pp. 120–145, May 2011, ISSN: 0924-9907, 1573-7683. DOI: 10.1007/s10851-010-0251-1. [Online]. Available: <http://link.springer.com/10.1007/s10851-010-0251-1> (visited on 04/12/2025).
- [8] K. H. Jin, M. T. McCann, E. Froustey, and M. Unser, “Deep convolutional neural network for inverse problems in imaging,” *IEEE Transactions on Image Processing*, vol. 26, no. 9, pp. 4509–4522, Sep. 2017, ISSN: 1941-0042. DOI: 10.1109/TIP.2017.2713099. [Online]. Available: <https://ieeexplore.ieee.org/document/7949028/> (visited on 04/12/2025).
- [9] R. Zha, Y. Zhang, and H. Li, “NAF: Neural attenuation fields for sparse-view CBCT reconstruction,” in *Medical Image Computing and Computer Assisted Intervention – MICCAI 2022*, L. Wang, Q. Dou, P. T. Fletcher, S. Speidel, and S. Li, Eds., Cham: Springer Nature Switzerland, 2022, pp. 442–452, ISBN: 978-3-031-16446-0. DOI: 10.1007/978-3-031-16446-0_42.
- [10] H. Shin, T. Kim, J. Lee, S. Y. Chun, S. Cho, and D. Shin, “Sparse-view CBCT reconstruction using meta-learned neural attenuation field and hash-encoding regularization,” *Computers in Biology and Medicine*, vol. 189, p. 109 900, May 1, 2025, ISSN: 0010-4825. DOI: 10.1016/j.compbiomed.2025.109900. [Online]. Available: <https://www.sciencedirect.com/science/article/pii/S0010482525002513> (visited on 04/12/2025).
- [11] R. Vo, J. Escoda, C. Vienne, and É. Decencière, “Plug-and-play learned proximal trajectory for 3d sparse-view x-ray computed tomography,” in *Computer Vision – ECCV 2024*, A. Leonardis, E. Ricci, S. Roth, O. Russakovsky, T. Sattler, and G. Varol, Eds., vol. 15093, Series Title: Lecture Notes in Computer Science, Cham: Springer Nature Switzerland, 2025, pp. 221–238. DOI: 10.1007/978-3-031-72761-0_13. [Online]. Available: https://link.springer.com/10.1007/978-3-031-72761-0_13 (visited on 04/12/2025).
- [12] J. Ho, A. Jain, and P. Abbeel, “Denoising diffusion probabilistic models,” in *Advances in Neural Information Processing Systems*, vol. 33, Curran Associates, Inc., 2020, pp. 6840–6851. [Online]. Available: <https://proceedings.neurips.cc/paper/2020/hash/4c5bfc8584af0d967f1ab10179ca4b-Abstract.html> (visited on 04/12/2025).
- [13] H. Chung, J. Kim, M. T. McCann, M. L. Klasky, and J. C. Ye, “Diffusion posterior sampling for general noisy inverse problems,” presented at the The Eleventh International Conference on Learning Representations, Sep. 29, 2022. [Online]. Available: <https://openreview.net/forum?id=OnD9zGAGT0k> (visited on 04/12/2025).
- [14] H. Chung, S. Lee, and J. C. Ye, “Decomposed diffusion sampler for accelerating large-scale inverse problems,” presented at the The Twelfth International Conference on Learning Representations, Oct. 13, 2023. [Online]. Available: <https://openreview.net/forum?id=DsEhQqtFAG> (visited on 04/12/2025).
- [15] B. Song, J. Hu, Z. Luo, J. A. Fessler, and L. Shen, “DiffusionBlend: Learning 3d image prior through position-aware diffusion score blending for 3d computed tomography reconstruction,” *Advances in Neural Information Processing Systems*, vol. 37, pp. 89 584–89 611, Dec. 16, 2024. [Online]. Available: https://proceedings.neurips.cc/paper_files/paper/2024/hash/a30769d9b62c9b94b72e21e0ca73f338-Abstract-Conference.html (visited on 04/12/2025).
- [16] E. Venkatesh and S. V. Elluru, “Cone beam computed tomography: Basics and applications in dentistry,” *Journal of Istanbul University Faculty of Dentistry*, vol. 51, no. 3, S102–S121, Dec. 2, 2017, ISSN: 2149-2352. DOI: 10.17096/jiufd.00289. [Online]. Available: <https://>

- //www.ncbi.nlm.nih.gov/pmc/articles/PMC5750833/ (visited on 04/14/2025).
- [17] A. Wagner, K. Schicho, F. Kainberger, W. Birkfellner, S. Grampp, and R. Ewers, "Quantification and clinical relevance of head motion during computed tomography," *Investigative Radiology*, vol. 38, no. 11, pp. 733–741, Nov. 2003, ISSN: 0020-9996. DOI: 10.1097/01.rli.0000084889.92250.b0.
 - [18] A. Wagner, K. Schicho, F. Kainberger, W. Birkfellner, S. Grampp, and R. Ewers, "Quantification and clinical relevance of head motion during computed tomography," *Investigative Radiology*, vol. 38, no. 11, pp. 733–741, Nov. 2003, ISSN: 0020-9996. DOI: 10.1097/01.rli.0000084889.92250.b0.
 - [19] A. Bousse, O. Bertolli, D. Atkinson, S. Arridge, S. Ourselin, B. F. Hutton, and K. Thielemans, "Maximum-likelihood joint image reconstruction/motion estimation in attenuation-corrected respiratory gated PET/CT using a single attenuation map," *IEEE transactions on medical imaging*, vol. 35, no. 1, pp. 217–228, 2015.
 - [20] T. Sun, J.-H. Kim, R. Fulton, and J. Nuyts, "An iterative projection-based motion estimation and compensation scheme for head x-ray CT," *Medical Physics*, vol. 43, no. 10, p. 5705, Oct. 2016, ISSN: 2473-4209. DOI: 10.1118/1.4963218.
 - [21] S. Ouadah, J. W. Stayman, G. J. Gang, T. Ehtiati, and J. H. Siewerdsen, "Self-calibration of cone-beam CT geometry using 3d–2d image registration," *Physics in medicine and biology*, vol. 61, no. 7, pp. 2613–2632, Apr. 7, 2016, ISSN: 0031-9155. DOI: 10.1088/0031-9155/61/7/2613. [Online]. Available: <https://www.ncbi.nlm.nih.gov/pmc/articles/PMC4948745/> (visited on 04/14/2025).
 - [22] M. Li, C. Lowe, A. Butler, P. Butler, and G. Wang, "Motion correction via locally linear embedding for helical photon-counting CT," in *7th International Conference on Image Formation in X-Ray Computed Tomography*, vol. 12304, SPIE, Oct. 17, 2022, pp. 559–567. DOI: 10.1117/12.2646714. [Online]. Available: <https://www.spiedigitallibrary.org/conference-proceedings-of-spie/12304/1230421/Motion-correction-via-locally-linear-embedding-for-helical-photon-counting/10.1117/12.2646714.full> (visited on 04/14/2025).
 - [23] A. Sisiniega, J. W. Stayman, J. Yorkston, J. H. Siewerdsen, and W. Zbijewski, "Motion compensation in extremity cone-beam CT using a penalized image sharpness criterion," *Physics in Medicine and Biology*, vol. 62, no. 9, pp. 3712–3734, May 7, 2017, ISSN: 1361-6560. DOI: 10.1088/1361-6560/aa6869.
 - [24] H. Huang, J. H. Siewerdsen, W. Zbijewski, C. R. Weiss, M. Unberath, T. Ehtiati, and A. Sisiniega, "Reference-free learning-based similarity metric for motion compensation in cone-beam CT," *Physics in Medicine and Biology*, vol. 67, no. 12, Jun. 16, 2022, ISSN: 1361-6560. DOI: 10.1088/1361-6560/ac749a.
 - [25] A. Preuhs, M. Manhart, P. Roser, E. Hoppe, Y. Huang, M. Psychogios, M. Kowarschik, and A. Maier, "Appearance learning for image-based motion estimation in tomography," *IEEE Transactions on Medical Imaging*, vol. 39, no. 11, pp. 3667–3678, Nov. 2020, ISSN: 1558-254X. DOI: 10.1109/TMI.2020.3002695. [Online]. Available: <https://ieeexplore.ieee.org/document/9117090> (visited on 04/14/2025).
 - [26] M. Thies, F. Wagner, N. Maul, H. Yu, M. Goldmann, L.-S. Schneider, M. Gu, S. Mei, L. Folle, A. Preuhs, M. Manhart, and A. Maier, "A gradient-based approach to fast and accurate head motion compensation in cone-beam CT," *IEEE Transactions on Medical Imaging*, vol. 44, no. 2, pp. 1098–1109, Feb. 2025, ISSN: 1558-254X. DOI: 10.1109/TMI.2024.3474250. [Online]. Available: <https://ieeexplore.ieee.org/document/10705329> (visited on 04/14/2025).
 - [27] T. Pengpen and M. Soleimani, "Motion-compensated cone beam computed tomography using a conjugate gradient least-squares algorithm and electrical impedance tomography imaging motion data," *Philosophical Transactions. Series A, Mathematical, Physical, and Engineering Sciences*, vol. 373, no. 2043, p. 20140390, Jun. 13, 2015, ISSN: 1471-2962. DOI: 10.1098/rsta.2014.0390.
 - [28] Q. Wu, X. Li, H. Wei, J. Yu, and Y. Zhang, "Joint rigid motion correction and sparse-view CT via self-calibrating neural field," in *2023 IEEE 20th International Symposium on Biomedical Imaging (ISBI)*, ISSN: 1945-8452, Apr. 2023, pp. 1–5. DOI: 10.1109/ISBI53787.2023.10230569. [Online]. Available: <https://ieeexplore.ieee.org/document/10230569> (visited on 04/14/2025).
 - [29] P. Dhariwal and A. Nichol, "Diffusion models beat GANs on image synthesis," *Advances in neural information processing systems*, vol. 34, pp. 8780–8794, 2021.
 - [30] A. Kazerouni, E. K. Aghdam, M. Heidari, R. Azad, M. Fayyaz, I. Hacıhaliloglu, and D. Merhof, "Diffusion models in medical imaging: A comprehensive survey," *Medical Image Analysis*, p. 102846, 2023.
 - [31] A. D. Pape, A. Bousse, C. Phung-Ngoc, and D. Visvikis, *Solving blind inverse problems: Adaptive diffusion models for motion-corrected sparse-view 4dct*, Feb. 1, 2025. DOI: 10.48550/arXiv.2501.12249. arXiv: 2501.12249[physics]. [Online]. Available: <http://arxiv.org/abs/2501.12249> (visited on 03/26/2025).
 - [32] H. Chung, S. Lee, and J. C. Ye, "Decomposed diffusion sampler for accelerating large-scale inverse problems," in *The Twelfth International Conference on Learning Representations*, 2024. [Online]. Available: <https://openreview.net/forum?id=DsEhqQtFAG>.
 - [33] I. A. Elbakri and J. A. Fessler, "Statistical image reconstruction for polyenergetic x-ray computed tomography," *IEEE Transactions on Medical Imaging*, vol. 21, no. 2, pp. 89–99, 2002.
 - [34] E. Y. Sidky, J. H. Jørgensen, and X. Pan, "Convex optimization problem prototyping for image reconstruction in computed tomography with the chambolle–pock algorithm," *Physics in Medicine & Biology*, vol. 57, no. 10, p. 3065, 2012.
 - [35] J. Ho, A. Jain, and P. Abbeel, "Denoising diffusion probabilistic models," *Advances in neural information processing systems*, vol. 33, pp. 6840–6851, 2020.
 - [36] J. Song, C. Meng, and S. Ermon, "Denoising diffusion implicit models," *arXiv preprint arXiv:2010.02502*, 2020.
 - [37] P. Friedrich, J. Wolleb, F. Bieder, A. Durrer, and P. C. Cattin, "WDM: 3D wavelet diffusion models for high-resolution medical image synthesis," in *MICCAI Workshop on Deep Generative Models*, Springer, 2024, pp. 11–21.
 - [38] Y. He, N. Murata, C.-H. Lai, Y. Takida, T. Uesaka, D. Kim, W.-H. Liao, Y. Mitsufuji, J. Z. Kolter, R. Salakhutdinov, et al., "Manifold preserving guided diffusion," *arXiv preprint arXiv:2311.16424*, 2023.
 - [39] Y. Zhu, K. Zhang, J. Liang, J. Cao, B. Wen, R. Timofte, and L. V. Gool, "Denoising diffusion models for plug-and-play image restoration," in *2023 IEEE/CVF Conference on Computer Vision and Pattern Recognition Workshops (CVPRW)*, Vancouver, BC, Canada: IEEE, Jun. 2023, pp. 1219–1229, ISBN: 979-8-3503-0249-3. DOI: 10.1109/CVPRW59228.2023.00129. [Online]. Available: <https://ieeexplore.ieee.org/document/10208800/> (visited on 04/02/2025).
 - [40] X. Jiang, G. J. Gang, and J. W. Stayman, "Multi-material decomposition using spectral diffusion posterior sampling," *arXiv preprint arXiv:2408.01519*, 2024.
 - [41] S. Chilamkurthy, R. Ghosh, S. Tanamala, M. Biviji, N. G. Campeau, V. K. Venugopal, V. Mahajan, P. Rao, and P. Warier, "Deep learning algorithms for detection of critical findings in head CT scans: A retrospective study," *The Lancet*, vol. 392, no. 10162, pp. 2388–2396, 2018.
 - [42] M. Ronchetti, "Torchradon: Fast differentiable routines for computed tomography," *arXiv preprint arXiv:2009.14788*, 2020.
 - [43] V. Gopalakrishnan and P. Golland, "Fast auto-differentiable digitally reconstructed radiographs for solving inverse problems in intraoperative imaging," in *Workshop on Clinical Image-Based Procedures*, Springer, 2022, pp. 1–11.